CCS Chemistry

RESEARCH ARTICLE

Received: Dec. 7, 2021 | Accepted: Feb. 4, 2022 | Published: Mar. 11, 2022

Room-Temperature Persistent Luminescence in Metal Halide Perovskite Nanocrystals for Solar-Driven CO_2 Bioreduction

Jie Wang[1†], Na Chen[1†], Wenjie Wang[2], Zhiheng Li[1], Bolong Huang[3], Yanbing Yang[1*] & Quan Yuan[1,2*]

[1]College of Chemistry and Molecular Sciences, School of Microelectronics, Wuhan University, Wuhan 430072, [2]Molecular Science and Biomedicine Laboratory (MBL), Institute of Chemical Biology and Nanomedicine, State Key Laboratory of Chemo/Biosensing and Chemometrics, College of Chemistry and Chemical Engineering, Hunan University, Changsha 410082, [3]Department of Applied Biology and Chemical Technology, The Hong Kong Polytechnic University, Hung Hom, Kowloon, Hong Kong SAR 999077

**Corresponding authors: yuanquan@whu.edu.cn; yangyanbing@whu.edu.cn; †J. Wang and N. Chen contributed equally to this work.*

Cite this: *CCS Chem.* **2023**, 5, 164–175
DOI: 10.31635/ccschem.022.202101694

The rapid crystal growth of metal halide perovskite (MHP) nanocrystals inevitably leads to the generation of abundant crystal defects in the lattice. Here, defects-mediated long-lived charges and accompanying room-temperature persistent luminescence are demonstrated to be a general phenomenon in MHP nanocrystals. Density functional theory calculations suggest that the collaboration of Schottky and point defects enables upward cascading depletion for electron transfer in MHP nanocrystals, leading to the generation of long-lived photoexcited charges with lifetimes over 30 min. The excellent optical properties including the presence of long-lived charges, high charge separation efficiency, and broad absorption in the visible region make MHPs ideal candidates for both photocatalysis and photobiocatalysis. The MHPs were further integrated with enzymes to construct a light-driven biosynthetic system for the selective production of fine chemicals from CO_2 with solar energy. The biosynthetic system can produce formate with a quantum yield of 3.24%, much higher than that of plants (~0.2–1.6%). These findings will benefit the understanding of the optoelectronic properties of MHPs and further provide opportunities for the development of biosynthetic systems for solar-to-chemical synthesis.

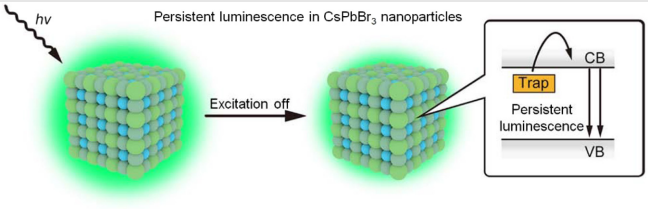

Keywords: **persistent luminescence, nanoparticles, metal halide perovskites, defects, CO_2 reduction**

Introduction

Metal halide perovskites (MHPs) have emerged as a fascinating class of semiconductors with superior optoelectronic properties, including a large light absorption coefficient, high charge mobility, long charge diffusion length, and tunable bandgaps.[1–4] In recent years, high-performance optoelectronics, such as solar cells,[5–7] light-emitting diodes (LEDs),[8] lasers,[9] and photodetectors,[1,2,10] have been developed based on MHPs.[4,11] Within the short

time since their development, perovskite solar cells have achieved power conversion efficiencies approaching that of commercialized polycrystalline silicon photovoltaics.[1,12] The optoelectronic properties of MHPs are highly correlated with their lattice structures.[13–15] Researchers have shown that regulating the lattice structures in MHPs by means such as doping[13–15] can change their crystalline structure, electronic structure, bandgap, and crystallinity of MHPs, leading to controllable quantum yields,[8] increased charge transport, and stability.[14–17] The lattice structure is one of the chief factors that determines the optoelectronic properties of MHPs.

Defects, the ubiquitous lattice structures in solid materials, are deviations or disruptions in the continuity of the regular arrangement of atoms.[18] The most exciting feature of MHPs is their defect tolerance,[1,2,4] indicating the presence of a large number of defects in MHPs.[19,20] Generally, the rapid crystal growth of MHPs inevitably leads to the generation of abundant defects in the lattice, such as vacancies and interstitials.[1,4,21] Defects in semiconductors have always been of paramount importance as they control the optoelectronic performance of these materials in applications.[22,23] The presence of defects can form transition levels in the bandgap and change the absorption/emission properties of semiconductors, leading to a substantial enhancement of the photoluminescence quantum yields or red shift of the emission peaks.[23,24] Also, defects can trap free charges and lead to the generation of long-lived charges with lifetimes up to hours.[23,25,26] The long-lived charges can recombine to produce persistent luminescence[26–28] or be transported to the surface of the semiconductors for photocatalysis.[23] The large number of unavoidable defects in MHPs also leads to modification of their bandgaps and the entrapment of free charges; that is, the defects empower MHPs with undiscovered optoelectronic properties.

Herein, we report that the intrinsic defects in MHPs can lead to long-lived charge separation and the persistent luminescence phenomenon, and the MHPs were integrated with enzymes for the selective production of fine chemicals from CO_2. Persistent luminescence was observed as a general phenomenon in MHPs due to the recombination of the long-lived charges after excitation ceases. The formation of different defects in $CsPbBr_3$ was studied with density functional theory (DFT) calculations, which indicated that the collaboration of Schottky defects and point defects supports the formation of long-lived charges based on the broad distribution of occupied energy levels within the bandgap. A light-driven biosynthetic system was further constructed for the production of fine chemicals from CO_2 based on $CsPbBr_3$ and enzymes. This biosynthetic system can produce formate from CO_2 continuously over light-dark cycles, demonstrating a promising route toward solar-to-chemical CO_2 reduction.

Experimental Methods

Materials

Lead(II) chloride ($PbCl_2$, 99.99%), lead(II) bromide ($PbBr_2$, 99.0%), lead(II) iodide (PbI_2, 99.9%), caesium carbonate (Cs_2CO_3, 99.9%), bismuth triiodide (BiI_3, 99.99%), silver nitrate ($AgNO_3$, 99.8%), oleic acid (OA, AR), 1-octadecene (ODE, 80–90%), oleylamine (OLA, AR), hydrobromic acid (HBr, AR, 40%), titanium butoxide (TBOT, ≥99.0%), triethanolamine (TEOA, AR), 2,2′-bipyridyl (AR, 99.0%), pentamethylcyclopentadienylrhodium(III) chloride dimer ($(Cp^*RhCl_2)_2$, 99%), and β-nicotinamide adenine dinucleotide (NAD^+, 97%) were purchased from Aladdin Reagent Co. Ltd. (Shanghai, China). Toluene (High Performance Liquid Chromatography grade) was purchased from Thermo Fisher Scientific, Inc. (Shanghai, China). Bismuth tribromide ($BiBr_3$, 99%) was purchased from Alfa Aesar Chemical Co. Ltd. (Shanghai, China). Methanol (AR, ≥ 99.7%), ethyl acetate (AR, ≥ 99.5%), *n*-hexane (AR, ≥ 97.0 %), and diethyl ether (AR, ≥ 99.5%) were purchased from Sinopharm Chemical Reagent Co., Ltd. (Shanghai, China). Formate dehydrogenase from Candida boidinii (CbFDH) and formate assay kit were purchased from Sigma-Aldrich Co., LLC. (Shanghai, China).

Characterization

The sizes and shapes of nanocrystals were determined by a transmission electron microscope (TEM) (JEOL, JEM-2100, Japan). The elemental mappings were conducted on a JEOL JEM-2100F TEM working at 200 kV. The shapes and elemental mappings of p-$CsPbBr_3$ were characterized by a field-emission scanning electron microscope (Zeiss Merlin Compact, Germany). Powder X-ray diffraction (XRD) characterization was conducted on a X-ray diffractometer (Burker, D8 Advance, Germany) with Cu-Kα radiation (λ = 1.5406 Å). Absorption spectra of nanocrystals were collected with a UV–vis absorbance spectrometer (Shimadzu, UV-2550, Japan). Photoluminescence spectra of nanocrystals were measured on a fluorescence spectrometer (Hitachi, FL4600, Japan). The afterglow luminescence in the $CsPbBr_3$ nanocrystal powder was collected on a fluorescence spectrometer (HORIBA Scientific, United States), Fluorolog-3-2ultrafast with 450 W xenon lamp, double mono in ex side, single mono (with H10330 NIR PMT as T-side) and iHR320 (with PPD-850 and CCD as L-side) in Em sides. The photoluminescence decay spectra were recorded on an fluorescence spectrometer (FLS980, Edinburgh Instruments) using the time-correlated single-photon counting mode. X-ray photoelectron spectroscopy (XPS) was analyzed using a X-ray photoelectron spectrometer (Escalab 250Xi, Thermo Fisher Scientific) equipped with Al Kα monochromatized X-rays at 1486.6 eV. The photoluminescence and persistent luminescence photos and videos were taken with a digital single-lens

DOI: 10.31635/ccschem.022.202101694
Citation: *CCS Chem.* **2023**, 5, 164–175
Link to VoR: https://doi.org/10.31635/ccschem.022.202101694

reflex camera (Nikon, D3000, Japan), and a portable ZF5 UV lamp was used as the excitation source.

DFT calculations

The CASTEP package within DFT was applied to perform the theoretical calculations for $CsPbBr_3$.[29] The generalized gradient approximation with Perdue–Burke–Ernzerhof was employed to show the exchange-correlation energy in all of the calculations.[30,31] The ultrasoft pseudopotential (cutoff energy, 310 eV) was used. The Broyden–Fletcher–Goldfarb–Shanno (BFGS) algorithm was employed to converge the Hellmann–Feynman forces to <0.001 eV/Å for all geometry optimization.[32] Guided by the initial convergence test, Monkhorst–Pack reciprocal space integration was conducted with coarse *k*-points in consideration of the DFT computational cost.[33] The ultrafine convergence criteria were set according to the tolerances of the interionic displacement, and the total energy did not exceed 5×10^{-3} Å per atom and 5×10^{-5} eV per atom, respectively.

Measurement of the afterglow decay images

A colloidal mixture of nanocrystals in *n*-hexane was placed in a 48-well plate. A portable ZF5 UV lamp was used as the excitation source. After illumination for 3 min, the decay images were recorded by using the IVIS Lumina XR Imaging System (Caliper, Peoria, IL, United States).

Photoelectrochemical measurement

The photoelectrochemical properties of p-$CsPbBr_3$ nanocrystals were measured on a CHI Model 618 C electrochemical workstation. A standard three-electrode system was used: fluorine-doped tin oxide glass coated with p-$CsPbBr_3$ nanocrystals as the working electrode, Pt plate as the counter electrode, and Ag/AgCl as the reference electrode. The 0.5 M Na_2SO_4 electrolyte solution was purged with high-purity argon for 30 min before each measurement. The photocurrent curves were recorded using a 300 W xenon lamp with switch on–off cycles.

Synthesis of Cs-oleate

A stock solution of Cs-oleate was synthesized following the reported synthesis procedure.[34] Briefly, 0.8145 g of Cs_2CO_3 (2.5 mmol), 2.5 mL of OA, and 40 mL of ODE were added to a 100 mL flask, followed by drying at 120 °C for 1 h under vacuum. After that, the solution in the flask was heated at 150 °C under argon gas. The solution became clear, and the obtained Cs-oleate was collected for further use.

Synthesis of $CsPbX_3$ nanocrystals

The $CsPbX_3$ perovskite nanocrystals were prepared according to a previously reported hot-injection method.[6] Briefly, 10 mL of ODE and 0.38 mmol of PbX_2 were added to a 50 mL three-neck round bottom flask, followed by drying for 1 h at 120 °C under vacuum. Then 1 mL of OLA and 1 mL of OA were injected into the above solution at 120 °C under argon gas. After PbX_2 was dissolved completely, the solution in the flask was heated at 160 °C. Then 1 mL of Cs-oleate solution preheated at 100 °C was quickly injected into the mixture. After 10 s of reaction, the flask was transferred to an ice-water bath for rapid cooling. The $CsPbX_3$ nanocrystals were collected by centrifugation.

Synthesis of $Cs_2AgBiBr_6$ nanocrystals

The $Cs_2AgBiBr_6$ nanocrystals were synthesized according to a reported procedure.[35] Briefly, 45 mg of $BiBr_3$, 17 mg of $AgNO_3$, 0.1 mL of HBr, 4 mL of ODE, 1 mL of OA, and 1 mL of OLA were loaded into a 25 mL three-neck round bottom flask and were heated at 120 °C for 1 h under vacuum. After that, the solution was heated at 200 °C in argon gas, and 0.8 mL of preheated Cs-oleate stock solution (100 °C) was quickly added into the solution under vigorous stirring. The color of the mixture quickly turned from yellow-green to yellow. A few seconds later, the flask was rapidly placed in an ice-water bath for cooling. The obtained $Cs_2AgBiBr_6$ nanocrystals were collected by centrifugation and redispersed in *n*-hexane.

Synthesis of $Cs_3Bi_2I_9$ nanocrystals

The $Cs_3Bi_2I_9$ nanocrystals were synthesized by a reported protocol.[36] The Cs-oleate precursor and the BiI_3 precursor were synthesized first. OA (1.5 mL), ODE (20 mL), and Cs_2CO_3 (0.45 g) were added to a 50 mL three-neck round bottom flask. The mixture was heated at 130 °C for 1 h with stirring under vacuum to form a clear colloidal Cs-oleate precursor. After that, OA (1.5 mL), OLA (1.5 mL), ODE (15 mL), and BiI_3 (330 mg) were added to a 50 mL three-neck round bottom flask. The mixture was dried under vacuum for 1 h at 90 °C to generate a yellow colloidal BiI_3 precursor. In a typical procedure, 2 mL of BiI_3 precursor in a glass vial was heated at 100 °C for 5 min. Then 0.1 mL of the preheated Cs-oleate solution was quickly added to the above solution. After about 40 s of reaction, the solution changed from yellow to deep orange, indicating the formation of $Cs_3Bi_2I_9$ nanocrystals. The $Cs_3Bi_2I_9$ nanocrystals were separated by centrifugation and redispersed in *n*-hexane.

Synthesis of p-$CsPbBr_3$ nanocrystals

The p-$CsPbBr_3$ nanocrystals were synthesized following the reported method.[37] First, the TBOT solution was prepared by dissolving 20 µL TBOT in 1 mL toluene, and the solution was added dropwise to 10 mL of $CsPbBr_3$ solution (about 2 mg/mL toluene) in a 50 mL centrifuge tube under stirring. The obtained solution was stirred at

DOI: 10.31635/ccschem.022.202101694
Citation: *CCS Chem.* **2023**, 5, 164–175
Link to VoR: https://doi.org/10.31635/ccschem.022.202101694

room temperature for hydrolysis until the clear solution became cloudy. After 3 h of reaction, the precipitate was separated by centrifugation, followed by drying at room temperature for 1 h and 80 °C overnight under vacuum. Subsequently, the dried yellow product was calcined at 300 °C for 5 h under argon flow. Finally, the p-$CsPbBr_3$ nanocrystals were ground in an agate mortar and stored in a centrifuge tube for further use.

Preparation of $[Cp^*Rh(bpy)H_2O]^{2+}$

Briefly, 30.90 mg of $(Cp^*RhCl_2)_2$ was suspended in 4 mL of methanol, and a red suspension was formed. Then 15.62 mg of 2,2′-bipyridyl was added to the red suspension, and a clear yellowish solution was obtained after a few minutes. The above yellowish solution was concentrated to about 1 mL by rotary evaporation. After that, [Cp*Rh(bpy)Cl]Cl was collected by adding diethyl ether to the concentrated solution at 4 °C and dried under vacuum conditions. A stock solution of $[Cp^*Rh(bpy)(H_2O)]^{2+}$ (50 mM) was prepared by adding [Cp*Rh(bpy)Cl]Cl to 1 mL of water and stored at 4 °C in the dark.

Photocatalytic regeneration of NADH

The photocatalytic reduction of NAD^+ into NADH (NADH = reduced form of nicotinamide-adenine dinucleotide) was conducted in a quartz reactor, and a 450 nm LED (50 W) was used to excite the solution. The photocatalytic reaction system (1 mL) contained 1 mM of NAD^+, 0.125 mM of $[Cp^*Rh(bpy)H_2O]^{2+}$, 2 M of TEOA, 0.5 mg/mL p-$CsPbBr_3$ and 100 mM phosphate buffer (PB, pH 7.5). The reaction system was incubated for 10 min in darkness before being illuminated by a 450 nm LED. The concentration of the regenerated NADH was determined by UV–vis spectrophotometry using 6220 M^{-1} cm^{-1} as the extinction coefficient of NADH at 340 nm. To optimize the catalytic performance of p-$CsPbBr_3$ nanocrystals, the pH values, sacrificial reagents, and the concentration of TEOA and $[Cp^*Rh(bpy)H_2O]^{2+}$ were manipulated.

Long persistent photocatalytic regeneration of NADH

The long persistent photocatalytic production of NADH was conducted with a similar protocol. First, p-$CsPbBr_3$ or TiO_2 nanoparticles (2 mg) dispersed in 0.2 mL of PB buffer (100 mM, pH 7.5) was illuminated by a 50 W 450 nm LED lamp for 2 h. Then, the irradiated solution was added to a reaction system composed of 1 mM of NAD^+, 0.125 mM of $[Cp^*Rh(bpy)H_2O]^{2+}$, 2 M of triethanolamine, and PB buffer. The final volume of the reaction system was 1 mL. The reaction system was incubated in the dark, and the amount of the regenerated NADH was determined by UV–vis spectrophotometry.

Biosynthesis of formate from CO_2

Briefly, the biosynthesis of the formate was conducted in a glass vial bubbled with CO_2 gas at room temperature, and a 50 W 450 nm LED was used as the light source. The reaction solution (2 mL) containing 2 mg/mL p-$CsPbBr_3$ or TiO_2 nanoparticles, 5 mM NAD^+, 0.125 mM of $[Cp^*Rh(bpy)H_2O]^{2+}$, 2 M of triethanolamine, 2 mg/mL CbFDH, and 100 mM PB buffer (pH 7.5) was bubbled with CO_2 gas. After illumination with a 450 nm LED for the designated time, the supernatant was collected by centrifugation. The concentration of formate in the supernatant was detected with the formate assay kit.

Biosynthesis of formate from CO_2 in light-dark cycles

The biosynthesis of formate with a light-dark cycle was carried out similarly to the above reaction. For the biosynthesis reaction under light illumination, a reaction system (2 mL) containing 2 mg/mL p-$CsPbBr_3$, 5 mM NAD^+, 0.125 mM of $[Cp^*Rh(bpy)H_2O]^{2+}$, 2 M of triethanolamine, and 100 mM PB buffer (pH 7.5) was loaded into a glass vial and illuminated with 450 nm LED lamp for a certain time. For the dark stage, 4 mg of CbFDH was added to the obtained solution, and the solution was bubbled with CO_2 gas in the dark at room temperature. The formate concentration was monitored by a formate assay kit. The artificial photosynthesis of the formate with four light-dark cycles was performed in a glass vial bubbled with CO_2 gas under the same reaction conditions.

Average photoluminescence lifetime calculation

The transient photoluminescence decay curves of $CsPbBr_3$ and p-$CsPbBr_3$ nanocrystals were fitted with a triplet-exponential function of $Y(t) = A_1\exp(-t/\tau_1) + A_2\exp(-t/\tau_2) + A_3\exp(-t/\tau_3) + y_0$, and the average photoluminescence lifetime (τ) of $CsPbX_3$ and p-$CsPbBr_3$ nanocrystals were calculated from eq 1:

$$\tau = \frac{A_1\tau_1^2 + A_2\tau_2^2 + A_3\tau_3^2}{A_1\tau_1 + A_2\tau_2 + A_3\tau_3}. \quad (1)$$

Quantum yield calculation

According to a previous study, the formate production quantum yield was calculated by the ratio of the effective electrons used for formate production to the total input photon flux[38]:

$$\text{Quantum yield}\,(\%) = \frac{2\times\text{mol of formate}}{\text{mol of total photons}}\times 100\%, \quad (2)$$

where mol of formate generated = the total formate concentration × total volume; mol of total photons = photo

DOI: 10.31635/ccschem.022.202101694
Citation: *CCS Chem.* **2023**, 5, 164–175
Link to VoR: https://doi.org/10.31635/ccschem.022.202101694

flux × area of illumination × reaction time/Avogadro's number (N_A).

And photo flux was estimated by eq 3:

$$\text{Photo flux} = \frac{P \times \lambda}{h \times c}, \quad (3)$$

where P is the power of the LED light, λ is the emission wavelength of the LED light, h is the Planck constant (6.63×10^{-34} J·s), and c is the speed of light (3.00×10^{8} m·s^{-1}).

Results and Discussion

The general persistent luminescence phenomenon in MHP nanocrystals

The defect-tolerance virtue of MHPs suggests the presence of abundant defects in them.[1,2,4] Considering the unique charge-trapping feature of crystal defects, we reason that the long-lived charges and the accompanying persistent luminescence occur in MHPs, as illustrated in Figure 1a. The classic cubic $CsPbBr_3$ nanocrystals[34] (Figure 1b) were first tested. As shown in Figure 1c, green persistent luminescence was observed from the $CsPbBr_3$ nanocrystal powder at room temperature after removing the 365 nm UV illumination (Supporting Information Video S1). Figure 1d further shows that obvious persistent luminescence at around 536 nm was detected in $CsPbBr_3$ nanocrystals even at a 5 s delay after photoexcitation at room temperature. We further recorded the persistent luminescence decay in $CsPbBr_3$ nanocrystals over time. Persistent luminescence with persistent time over 300 s was detected in $CsPbBr_3$ nanocrystals (Figure 1e), suggesting the presence of long-lived charges in $CsPbBr_3$. These results confirm that long-lived charges and the accompanying persistent luminescence occurred in the $CsPbBr_3$ nanocrystals.

We next asked whether persistent luminescence is a general phenomenon in MHP nanocrystals. A series of perovskite nanocrystals were further tested, including $CsPbX_3$ (X= Cl–I),[34] $Cs_2AgBiBr_6$,[35] and $Cs_3Bi_2I_9$[36] (Supporting Information Figures S1–S8). The persistent luminescence feature of these perovskite nanocrystals was tested. Figure 1f presents the room-temperature phosphorescence spectra of the MHP nanocrystals. Long-lifetime emissions were observed over the entire

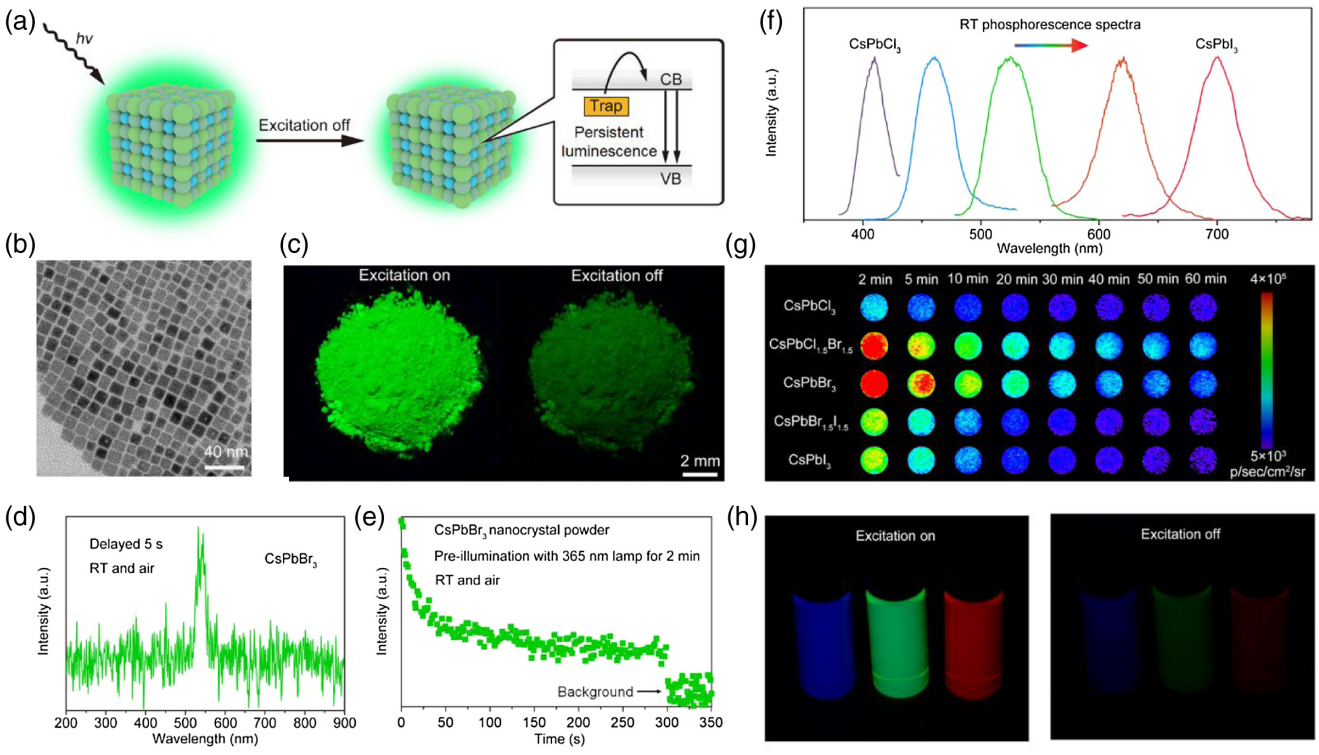

Figure 1 | *Persistent luminescence in MHP nanocrystals. (a) Schematic representation for the persistent luminescence in MHP nanocrystals. (b) TEM image of the $CsPbBr_3$ nanocrystals. (c) Photographs of $CsPbBr_3$ nanocrystal powder during and after excitation. (d) Room-temperature persistent luminescence spectrum of the $CsPbBr_3$ nanocrystals with a delay time of 5 s. (e) Persistent luminescence decay curve of the $CsPbBr_3$ nanocrystals pre-excited by a UV lamp for 2 min. (f) Room-temperature phosphorescence spectra of the MHP nanocrystals with varying halide compositions. (g) Persistent luminescence decay images in MHP nanocrystals. (h) Photographs of $CsPbCl_{1.5}Br_{1.5}$, $CsPbBr_3$, and $CsPbBr_{1.5}I_{1.5}$ colloidal dispersions during and after excitation.*

DOI: 10.31635/ccschem.022.202101694
Citation: *CCS Chem.* **2023**, 5, 164–175
Link to VoR: https://doi.org/10.31635/ccschem.022.202101694

visible spectral region from the MHP nanocrystal dispersions, indicating the persistent luminescence feature of these nanocrystals. The persistent luminescence in the MHP nanocrystals was further studied using the IVIS Spectrum imaging system[39] in the bioluminescence mode. After precharging with a 365 nm UV lamp for 2 min, all of the MHP nanocrystals displayed strong persistent luminescence after excitation ceases (Figure 1g and Supporting Information Figure S9). The decay images in Figure 1g show that the persistent luminescence intensities of the MHP nanocrystals decreased slowly and that obvious persistent luminescence was still detected after 1 h of decay. Photographs of $CsPbX_3$ colloidal dispersions during and after excitation at room temperature show obvious persistent luminescence (Figure 1h and Supporting Information Video S2). These assays demonstrate that the long-lived charges and the accompanying persistent luminescence are a general phenomenon in MHPs.

The origin of the persistent luminescence phenomenon in MHP nanocrystals

The persistent luminescence originates from the slow escape and recombination of the charges trapped by defects in MHP nanocrystals after excitation ceases. The formation of defects in $CsPbBr_3$ and their influences on charge separation were further systematically studied via their electronic structures. In $CsPbBr_3$ crystal, both the bonding and antibonding orbitals near the Fermi level (E_F) are predominantly contributed to by Pb (Figure 2a). The Br sites also display the electron-rich feature while Cs atoms show a limited contribution to the electronic distribution (Figure 2a). From the projected density of states, the conduction band minimum (CBM) and valence band maximum (VBM) are both mainly composed of the p-orbitals from Pb-6p and Br-4p (Figure 2b). Previous studies have demonstrated the presence of both defects-related shallow and deep trap states in MHPs.[19,20] The formation of commonly encountered native defects such as vacancies and their influence on the optical properties of $CsPbBr_3$ was systematically studied with DFT calculations. For the formation of point defects in $CsPbBr_3$ crystals, the pure vacancies show slightly higher energy costs while the antisite and Frenkel defects were thermodynamically favorable, indicating the presence of unavoidable defects in $CsPbBr_3$ crystals during synthesis (Figure 2c). The single-particle levels of intrinsic defects in $CsPbBr_3$ with different charge states are further summarized. Figure 2d indicates that the point defects are responsible for the formation of the hole traps near the VBM. For the Pb vacancy (V_{Pb}), the occupied states were noted in both V_{Pb}^{0} and V_{Pb}^{2-}, which are 0.31 and 0.33 eV above the VBM, respectively. Meanwhile, an empty state at 0.27 eV above the VBM was identified in the neutral V_{Pb}^{-}, which can alleviate the energy barrier for electron transfer from the conduction band. The additional gap states for V_{Cs}^{0} and V_{Cs}^{-} were noticed at 0.53 and 0.31 eV above the VBM, respectively. In particular, we noticed the ladder-like distributions of occupied states from Pb_i^{0} to Pb_i^{2+}, which varies from the range of 0.5–2.16 eV above the VBM. These states have supplied the nonequilibrium intrinsic charge states to prolong the luminescence performance after excitation. Moreover, large amounts of occupied states have been formed within the range of 0.6 eV by both the anion and cation Frenkel defects. Therefore, we propose the upward cascading depletion mechanism facilitated by high energy levels of defects from the synthesis. Under excitation, electrons trapped in these states can tunnel through the conduction band to realize deexcitation and accompanying persistent luminescence.

Besides the simple point defects, Schottky and Schottky-like defects were further investigated in agglomerated and separated types (Figure 2e). Both the Schottky and the Schottky-like defects such as PbBr vacancy (V_{PbBr2}) introduce empty gap states above the VBM. For instance, for the agglomerated STK defects (STK-1), two additional electron traps were formed at the CBM, which located at 2.49 and 2.89 eV above VBM, respectively. These two electron traps correspond to photon emission of 498 (violet) and 429 nm (blue), which were close to the experimental results. Similar to the agglomerated STK, the separated STK defect also demonstrated two-gap states at 2.50 and 2.07 eV above VBM, supporting the photoemission of 496 (blue) and 598 nm (orange), respectively. These additional empty states not only act as electron traps but also promote upward cascading depletion-based electron transfer by supplying the appropriate energy levels over the CBM. Therefore, combined with the upward cascading depletion by point defects, the intrinsic defects can lead to the generation of long-lived charges and persistent luminescence in $CsPbBr_3$ crystals. In addition to the intrinsic defects, introducing exogenous defects by means such as heterovalence doping during preparation can further enhance the intensity and prolong the decay time of persistent luminescence in MHPs.[25,27]

Light-driven biosynthesis of formate from CO_2 based on MHPs

The presence of long-lived charges, efficient charge separation, and broad visible absorption strongly indicate the potential application of MHP nanocrystals in photocatalysis and solar-to-chemical synthesis.[38,40–43] A light-driven biosynthetic system with a simple electron conduit was further constructed for the production of fine chemicals from CO_2 based on $CsPbBr_3$ nanocrystals and enzymes (Figure 3a). This biosynthetic system integrates the highly efficient light-harvesting ability and long-lived charges of $CsPbBr_3$ nanocrystals with the highly specific CO_2-processing capability of enzymes.[38,44,45] The $CsPbBr_3$ nanocrystals were passivated by a TiO_2 shell

DOI: 10.31635/ccschem.022.202101694
Citation: *CCS Chem.* **2023**, 5, 164–175
Link to VoR: https://doi.org/10.31635/ccschem.022.202101694

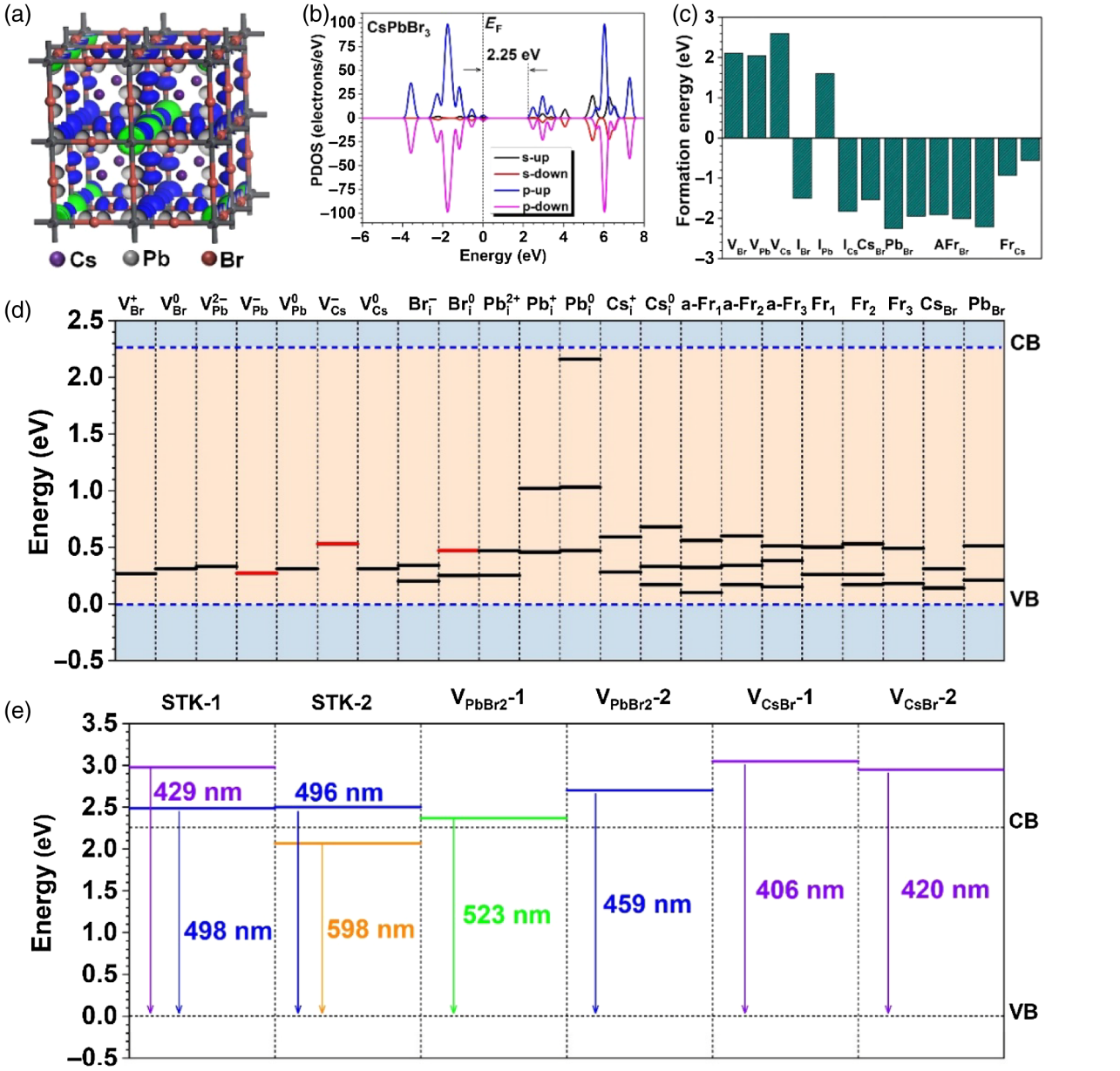

Figure 2 | *The origin of persistent luminescence in $CsPbBr_3$. (a) The bonding and antibonding orbitals of $CsPbBr_3$. Purple balls, Cs; dark grey balls, Pb; brown balls, Br; blue isosurface, bonding orbitals; green isosurface, antibonding orbitals. (b) The projected density of states of $CsPbBr_3$. (c) Formation energies of point defect in $CsPbBr_3$. (d) The summarized single-particle levels of simple point defects of $CsPbBr_3$ in both charged and neutral states (empty states = red; occupied states = black). (e) The summarized single-particle levels of Schottky and Schottky-like defects of $CsPbBr_3$ in agglomerated and separation types. STK-1, V_{PbBr2}-1, and V_{CsBr}-1 are the agglomerated type, and STK-2, V_{PbBr2}-2, and V_{CsBr}-2 are the separated type of defects.*

(named as p-$CsPbBr_3$)[37] to protect $CsPbBr_3$ from degradation and to facilitate charge transfer (Supporting Information Figures S10–S12). Compared with $CsPbBr_3$, the p-$CsPbBr_3$ shows a faster photoluminescence decay and weaker persistent luminescence intensities, suggesting the efficient transfer of electrons from $CsPbBr_3$ to the TiO_2 shell (Supporting Information Figures S13 and S14). Under visible light, the generated long-lived electrons in $CsPbBr_3$ nanocrystals pass through TiO_2 and reach the electron shuttle $[Cp^*Rh(bpy)H_2O]^{2+}$ (Supporting Information Figures S15 and S16). The reduced form electron shuttle $[Cp^*Rh(bpy)]^+$ further shuttles the electrons to NAD^+, which converts the NAD^+ to the reduced form, NADH, one of the major reducing agents in biosynthesis. The NADH is consumed in the reduction of CO_2 to formate, and the released NAD^+ oxidizes the $[Cp^*Rh(bpy)]^+$ for the cyclic production of NADH. By this simple electron conduit, the

DOI: 10.31635/ccschem.022.202101694
Citation: *CCS Chem.* **2023**, 5, 164–175
Link to VoR: https://doi.org/10.31635/ccschem.022.202101694

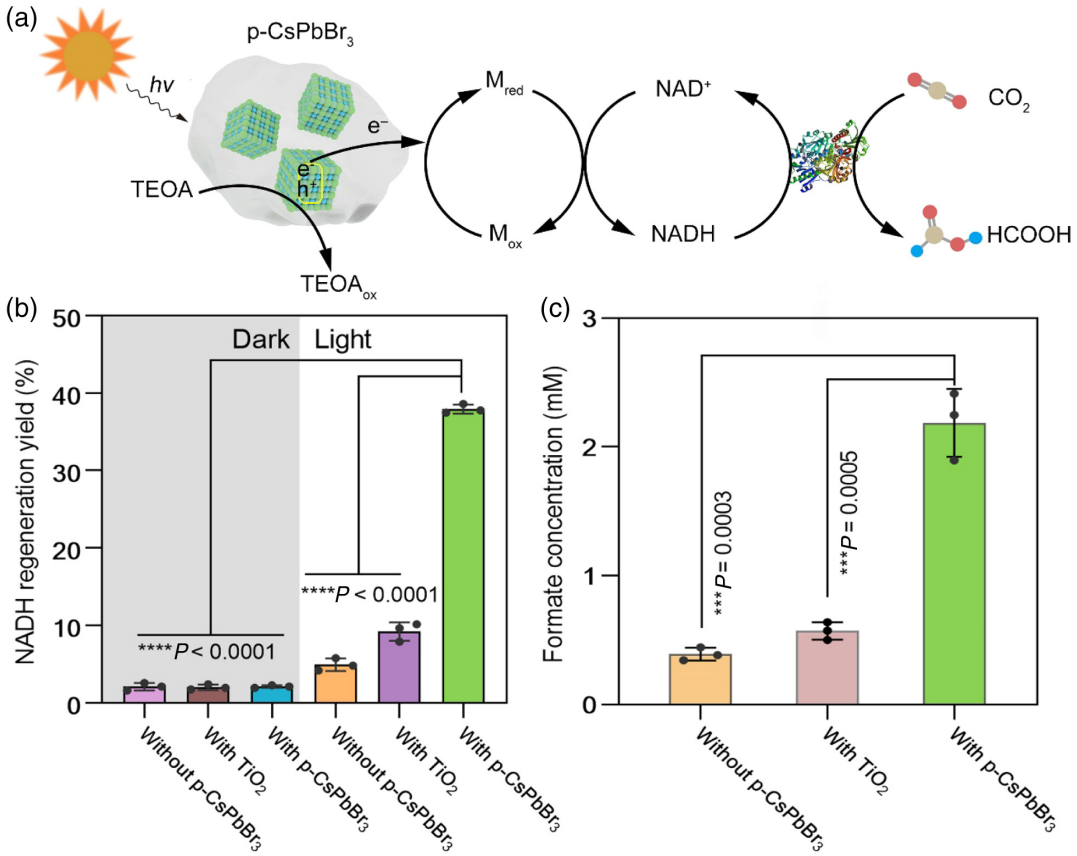

Figure 3 | *Light-driven biosynthesis of formate from CO_2. (a) Schematic illustration of the light-driven biosynthetic system based on p-$CsPbBr_3$ and formate dehydrogenase (CbFDH). Mox, $[Cp^*Rh(bpy)H_2O]^{2+}$. Mred, $[Cp^*Rh(bpy)]^{+}$. TEOA, triethanolamine. (b) Photocatalytic regeneration of NADH by a 450 nm LED (50 W) illumination. (c) Production of formate from CO_2 under LED (50 W) illumination. Error bars show the mean ± standard error of the mean (s.e.m.) of three independent measurements.*

light-driven biosynthetic system can channel the photogenerated electrons from p-$CsPbBr_3$ to produce NADH for the sustainable conversion of CO_2 into high-value chemicals. As shown in Figure 3b, the light-driven biosynthetic system afforded a much higher NADH regeneration yield compared to the group without the p-$CsPbBr_3$. The favorably oriented electron transfer in the light-driven biosynthetic system provides an NADH production rate of 304.5 ± 5.2 μmol g^{-1} h^{-1}, corresponding to a yield of 37.9 ± 0.6%. Figure 3c further shows a pronounced increase in formate production. Moreover, the light-driven biosynthetic system produced 2.19 ± 0.29 mM formate under visible light illumination for 2 h, much more than the system without p-$CsPbBr_3$ nanocrystals. Collectively, these results demonstrate that high-value chemicals can be efficiently produced from CO_2 by integrating the MHP nanocrystals with an established biosynthetic pathway. The developed light-driven biosynthetic system can serve as a promising method to realize solar-to-chemical conversion.

NADH and formate production by the light-driven biosynthetic system

A series of biosynthetic tests were performed to investigate the NADH and formate generation under light illumination (Supporting Information Figure S17). Transient photocurrent measurement was employed to assay the electron-donating performance of the p-$CsPbBr_3$ nanocrystals since electrons transferred out of the p-$CsPbBr_3$ could be easily captured by an electrode.[46] Under illumination by a 300 W xenon lamp, p-$CsPbBr_3$ produced a robust cathodic photocurrent with a density of about 1.33 μA cm^{-2}, much higher than that of bare TiO_2, showing the good electron-donating feature of p-$CsPbBr_3$ (Supporting Information Figure S18). Figure 4a shows that the yield of NADH increased nearly linearly over time under LED (450 nm) illumination, and the yield reached 37.9% within 2.5 h. The NADH regeneration rate was determined to be 304.5 ± 5.2 μmol g^{-1} h^{-1}, nearly 769.6% higher than that of the bare TiO_2 and the control group without the p-$CsPbBr_3$ nanocrystals (Supporting

DOI: 10.31635/ccschem.022.202101694
Citation: *CCS Chem.* **2023**, 5, 164–175
Link to VoR: https://doi.org/10.31635/ccschem.022.202101694

Information Figure S19). The NADH regeneration yield increased gradually with the increase of the sacrificial hole scavenger TEOA concentration (Supporting Information Figure S20). The optimal pH for the photogeneration of NADH was determined to be about 7.5 (Supporting Information Figure S20). Moreover, the light-driven biosynthetic system displayed good recycling capability in the photogeneration of NADH. Compared with the first cycle, the system retained an NADH regeneration yield of 93% in the tenth cycle (Supporting Information Figure S21), indicating the good reusability of the p-$CsPbBr_3$ in the photocatalytic process.

The MHP nanocrystals can store photon energy within the defects in the form of long-lived charges with a lifetime of over minutes. Beyond recombination of the trapped charges to produce persistent luminescence, the trapped charges in p-$CsPbBr_3$ nanocrystals can also pass to the electron shuttle $[Cp^*Rh(bpy)H_2O]^{2+}$ for the production of NADH in the dark. The p-$CsPbBr_3$ nanocrystals pre-illuminated with the LED for 30 min were added to the biosynthetic system for the conversion of NAD^+ into NADH in the dark. Figure 4b shows that the reaction system displays obvious NADH generation, indicating that the long-lived electrons in p-$CsPbBr_3$ nanocrystals can be used for biosynthesis after excitation ceases. The above findings suggest the special ability of the MHP nanocrystals in storing the photon energy within defects for photocatalysis in the dark as well as their capability to continuously produce high-value chemicals from CO_2 throughout the day-night cycles in nature.

The formate production from CO_2 was further investigated under visible light illumination. As shown in Figure 4c, the production of formate gradually increased over reaction time in the biosynthetic system, and the amount of produced formate reached 4.38 μmol after 2 h, affording a formate production quantum yield of 3.24 ± 0.21%. To further study the formate production capability of the light-driven biosynthetic system, the system was illuminated with visible light for different times, followed by 1 h of reaction in the dark. The produced formate increased with the prolonged illumination time (Supporting Information Figure S22), which can be ascribed to the gradual accumulation of NADH in the biosynthetic system with increasing illumination time. To further study the photosynthetic behavior, the light-driven biosynthetic system was illuminated in four

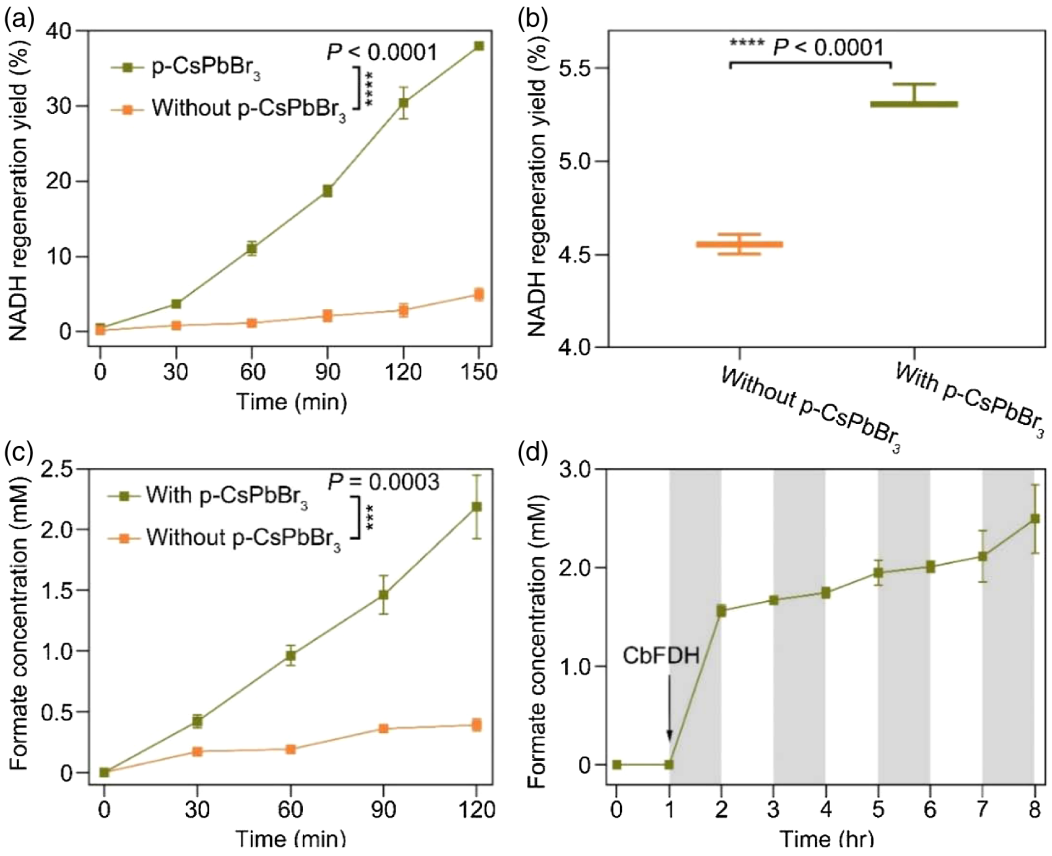

Figure 4 | *The NADH and formate generation in the light-driven biosynthetic system. (a) Light-driven NADH generation yield over time. (b) Regeneration of NADH in the dark with pre-illuminated p-$CsPbBr_3$ nanocrystals. (c) Light-driven formate generation vs time. (d) Light-driven formate production with light-dark cycles. Error bars show the mean ± standard error of the mean (s.e.m.) of three independent measurements.*

DOI: 10.31635/ccschem.022.202101694
Citation: *CCS Chem.* **2023**, 5, 164–175
Link to VoR: https://doi.org/10.31635/ccschem.022.202101694

alternating light-dark cycles of 1 h illumination/1 h dark, to imitate the intermittent nature of the solar source. The biosynthetic system continuously produced formate during the light-dark cycles, and a quantum yield of 1.85 ± 0.29% was finally achieved (Figure 4d). These findings thus provide strong evidence for the good promise of MHPs in solar-to-chemical conversion by integrating their superior optoelectronic properties with the biosynthetic pathways in nature.

Conclusion

We have demonstrated the long-lived charges and the accompanying persistent luminescence in MHPs. DFT calculations confirm that the point and Schottky defects in the nanocrystals supply abundant occupied states near the CBM, and the persistent luminescence in MHPs is produced with the upward cascading depletion mechanism. An MHPs-based light-driven biosynthetic system was further constructed for the production of fine chemicals from CO_2 by integrating the superior optoelectronic properties of MHPs with the CO_2-processing capability of enzymes. This investigation demonstrates the generation of long-lived charges in MHP nanocrystals, and also offers an opportunity for developing light-driven biosynthetic systems to produce high-value chemicals with solar energy. Moreover, beyond the development of advanced solar-to-chemical synthesis systems, the defects-associated long-lived charges establish further avenues for applications of MHPs in artificial photosynthesis and renewable solar fuel production.

Supporting Information

Supporting Information is available and includes TEM images of the nanoparticles, photos of the MHP nanoparticle dispersions, XRD analysis of the MHP nanoparticles, absorption and photoluminescence spectra (solid line) of the MHP nanoparticles, persistent luminescence decay images of the MHP nanoparticles, XPS analysis of the p-$CsPbBr_3$ nanocrystals, synthesis procedure of the Rh-based electron shuttle M, the electron transfer process in the light-driven biosynthetic system, photocurrent analysis of the nanoparticles, and the light-driven NADH and formate generation under different conditions.

Conflict of Interest

The authors declare no competing interests.

Acknowledgments

This work was supported by the National Natural Science Foundation of China (nos. 21925401 and 21904100) and the National Key R&D Program of China (no. 2017YFA0208000). Q.Y. and Y.Y. thank the large-scale instrument and equipment-sharing foundation of Wuhan University.

References

1. Liu, X. K.; Xu, W. D.; Bai, S.; Jin, Y. Z.; Wang, J. P.; Friend, R. H.; Gao, F. Metal Halide Perovskites for Light-Emitting Diodes. *Nat. Mater.* **2021**, *20*, 10–21.
2. Quan, L. N.; Rand, B. P.; Friend, R. H.; Mhaisalkar, S. G.; Lee, T.; Sargent, E. H. Perovskites for Next-Generation Optical Sources. *Chem. Rev.* **2019**, *119*, 7444–7477.
3. Luo, D. Y.; Yang, W. Q.; Wang, Z. P.; Sadhanala, A.; Hu, Q.; Su, R.; Shivanna, R.; Trindade, G. F.; Watts, J. F.; Xu, Z. J.; Liu, T. H.; Chen, K.; Ye, F. J; Wu, P.; Zhao, L. C.; Wu, J.; Tu, Y. G.; Zhang, Y. F.; Yang, X. Y.; Zhang, W.; Friend, R. H.; Gong, Q. H.; Snaith, H. J.; Zhu, R. Enhanced Photovoltage for Inverted Planar Heterojunction Perovskite Solar Cells. *Science* **2018**, *360*, 1442–1446.
4. Shi, E. Z.; Yuan, B.; Shiring, S. B.; Gao, Y.; Akriti; Guo, Y. F.; Su, C.; Lai, M. L.; Yang, P. D.; Kong, J.; Savoie, B. M.; Yu, Y.; Dou, L. T. Two-Dimensional Halide Perovskite Lateral Epitaxial Heterostructures. *Nature* **2020**, *580*, 614–620.
5. Liu, Y. G.; Akin, S.; Pan, L. F.; Uchida, R.; Milic, J. V.; Hinderhofer, A.; Schreiber, F.; Uhl, A. R.; Zakeeruddin, S. M.; Hagfeldt, A.; Dar, M. I.; Grätzel, M. Ultrahydrophobic 3D/2D Fluoroarene Bilayer-Based Water-Resistant Perovskite Solar Cells with Efficiencies Exceeding 22%. *Sci. Adv.* **2019**, *5*, eaaw2543.
6. Wang, R.; Mujahid, M.; Duan, Y.; Wang, Z. K.; Xue, J. J.; Yang, Y. A Review of Perovskites Solar Cell Stability. *Adv. Funct. Mater.* **2019**, *29*, 1808843.
7. Ni, Z.; Bao, C. X.; Liu, Y.; Jiang, Q.; Wu, W. Q.; Chen, S. S.; Dai, X. Z.; Chen, B.; Hartweg, B.; Yu, Z. S.; Holman, Z.; Huang, J. S. Resolving Spatial and Energetic Distributions of Trap States in Metal Halide Perovskite Solar Cells. *Science* **2020**, *367*, 1352–1358.
8. Quan, L. N.; García de Arquer, F. P.; Sabatini, R. P.; Sargent, E. H. Perovskites for Light Emission. *Adv. Mater.* **2018**, *30*, 1801996.
9. Xing, G. C.; Mathews, N.; Lim, S. S.; Yantara, N.; Liu, X. F.; Sabba, D.; Grätzel, M.; Mhaisalkar, S.; Sum, T. C. Low-Temperature Solution-Processed Wavelength-Tunable Perovskites for Lasing. *Nat. Mater.* **2014**, *13*, 476–480.
10. Chen, Q. S.; Wu, J.; Ou, X. Y.; Huang, B. L.; Almutlaq, J.; Zhumekenov, A. A.; Guan, X. W.; Han, S. Y.; Liang, L. L.; Yi, Z. G.; Li, J.; Xie, X. J.; Wang, Y.; Li, Y.; Fan, D. Y.; Teh, D. B. L.; All, A. H.; Mohammed, O. F.; Bakr, O. M.; Wu, T.; Bettinelli, M.; Yang, H. H.; Huang, W.; Liu, X. G. All-Inorganic Perovskite Nanocrystal Scintillators. *Nature* **2018**, *561*, 88–93.
11. Wang, Z. P.; Lin, Q. Q.; Wenger, B.; Christoforo, M. G.; Lin, Y. H.; Klug, M. T.; Johnston, M. B.; Herz, L. M.; Snaith, H. J. High Irradiance Performance of Metal Halide Perovskites for Concentrator Photovoltaics. *Nat. Energy* **2018**, *3*, 855–861.

DOI: 10.31635/ccschem.022.202101694
Citation: *CCS Chem.* **2023**, 5, 164–175
Link to VoR: https://doi.org/10.31635/ccschem.022.202101694

12. Wang, K.; Yang, D.; Wu, C. C.; Shapter, J.; Priya, S. Mono-Crystalline Perovskite Photovoltaics toward Ultrahigh Efficiency? *Joule* **2019**, *3*, 311–316.
13. Saidaminov, M. I.; Kim, J.; Jain, A.; Quintero-Bermudez, R.; Tan, H. R.; Long, G. K.; Tan, F. R.; Johnston, A.; Zhao, Y. C.; Voznyy, O.; Sargent, E. H. Suppression of Atomic Vacancies via Incorporation of Isovalent Small Ions to Increase the Stability of Halide Perovskite Solar Cells in Ambient Air. *Nat. Energy* **2018**, *3*, 648–654.
14. Abdi-Jalebi, M.; Andaji-Garmaroudi, Z.; Cacovich, S.; Stavrakas, C.; Philippe, B.; Richter, J. M.; Alsari, M.; Booker, E. P.; Hutter, E. M.; Pearson, A. J.; Lilliu, S.; Savenije, T. J.; Rensmo, H.; Divitini, G.; Ducati, C.; Friend, R. H.; Stranks, S. D. Maximizing and Stabilizing Luminescence from Halide Perovskites with Potassium Passivation. *Nature* **2018**, *555*, 497–501.
15. Zou, S. H.; Liu, Y. S.; Li, J. H.; Liu, C. P.; Feng, R.; Jiang, F. L.; Li, Y. X.; Song, J. Z.; Zeng, H. B.; Hong, M. C.; Chen, X. Y. Stabilizing Cesium Lead Halide Perovskite Lattice through Mn (II) Substitution for Air-Stable Light-Emitting Diodes. *J. Am. Chem. Soc.* **2017**, *139*, 11443–11450.
16. Almeida, G.; Infante, I.; Manna, L. Resurfacing Halide Perovskite Nanocrystals. *Science* **2019**, *364*, 833–834.
17. Fang, Z.; Shang, M. H.; Hou, X. M.; Zheng, Y. P.; Du, Z. T.; Yang, Z. B.; Chou, K. C.; Yang, W. Y.; Wang, Z. L.; Yang, Y. Bandgap Alignment of α-$CsPbI_3$ Perovskites with Synergistically Enhanced Stability and Optical Performance via B-Site Minor Doping. *Nano Energy* **2019**, *61*, 389–396.
18. Bollmann, W. *Crystal Defects and Crystalline Interfaces*; Springer: Berlin, **1970**.
19. Motti, S. G.; Meggiolaro, D.; Martani, S.; Sorrentino, R.; Barker, A. J.; Angelis, F. D.; Petrozza, A. Defect Activity in Lead Halide Perovskites. *Adv. Mater.* **2019**, *31*, 1901183.
20. Seth, S.; Ahmed, T.; De, A.; Samanta, A. Tackling the Defects, Stability, and Photoluminescence of $CsPbX_3$ Perovskite Nanocrystals. *ACS Energy Lett.* **2019**, *4*, 1610–1618.
21. Huang, H.; Bodnarchuk, M. I.; Kershaw, S. V.; Kovalenko, M. V.; Rogach, A. L. Lead Halide Perovskite Nanocrystals in the Research Spotlight: Stability and Defect Tolerance. *ACS Energy Lett.* **2017**, *2*, 2071–2083.
22. Wang, D.; Li, X. B.; Han, D.; Tian, W. Q.; Sun, H. B. Engineering Two-Dimensional Electronics by Semiconductor Defects. *Nano Today* **2017**, *16*, 30–45.
23. Lin, Q. S.; Li, Z. H.; Yuan, Q. Recent Advances in Autofluorescence-Free Biosensing and Bioimaging Based on Persistent Luminescence Nanoparticles. *Chin. Chem. Lett.* **2019**, *30*, 1547–1556.
24. Ono, L. K.; Liu, S. Z.; Qi, Y. B. Reducing Detrimental Defects for High-Performance Metal Halide Perovskite Solar Cells. *Angew. Chem. Int. Ed.* **2019**, *59*, 6676–6698.
25. Wang, J.; Ma, Q. Q.; Hu, X. X.; Liu, H. Y.; Zheng, W.; Chen, X. Y.; Yuan, Q.; Tan, W. H. Autofluorescence-Free Targeted Tumor Imaging Based on Luminous Nanoparticles with Composition-Dependent Size and Persistent Luminescence. *ACS Nano* **2017**, *11*, 8010–8017.
26. Ou, X. Y.; Qin, X.; Huang, B. L.; Zan, J.; Wu, Q. X.; Hong, Z. Z.; Xie, L. L.; Bian, H. Y.; Yi, Z. G.; Chen, X. F.; Wu, Y. M.; Song, X. R.; Li, J.; Chen, Q. S.; Yang, H. H.; Liu, X. G. High-Resolution X-Ray Luminescence Extension Imaging. *Nature* **2021**, *590*, 410–415.
27. Tian, M.; Gao, Y.; Zhou, P. Y.; Chi, K.; Zhang, Y.; Liu, B. Improving Persistent Luminescence in Pressure-Tuned $CsPbBr_3$ Nanocrystals by Ce^{3+} Doping. *Phys. Chem. Chem. Phys.* **2021**, *23*, 20567–20573.
28. Zhang, H.; Yang, Z.; Zhao, L.; Cao, J. Y.; Yu, X.; Yang, Y.; Yu, S. F.; Qiu, J. B.; Xu, X. H. Long Persistent Luminescence from All-Inorganic Perovskite Nanocrystals. *Adv. Optical Mater.* **2020**, *8*, 2000585.
29. Clark, S. J.; Segallii, M. D.; Pickardii, C. J.; Hasnipiii, P. J.; Probertiv, M. I. J. First Principles Methods Using CASTEP. *Zeitschrift für Kristallographie* **2005**, *220*, 567–570.
30. Perdew, J. P.; Burke, K.; Ernzerhof, M. Generalized Gradient Approximation Made Simple. *Phys. Rev. Lett.* **1996**, *77*, 3865–3868.
31. Perdew, J. P.; Chevary, J. A.; Vosko, S. H.; Jackson, K. A.; Pederson, M. R.; Singh, D. J.; Fiolhais, C. Atoms, Molecules, Solids, and Surfaces: Applications of the Generalized Gradient Approximation for Exchange and Correlation. *Phy. Rev. B* **1992**, *46*, 6671–6687.
32. Head, J. D.; Zerner, M. C. A Broyden-Fletcher-Goldfarb-Shanno Optimization Procedure for Molecular Geometries. *Chem. Phys. Lett.* **1985**, *122*, 264–270.
33. Probert, M. I. J.; Payne, M. C. Improving the Convergence of Defect Calculations in Supercells—An Ab Initio Study of the Neutral Silicon Vacancy. *Phys. Rev. B* **2003**, *67*, 075204.
34. Protesescu, L.; Yakunin, S.; Bodnarchuk, M. I.; Krieg, F.; Caputo, R.; Hendon, C. H.; Yang, R. X.; Walsh, A.; Kovalenko, M. V. Nanocrystals of Cesium Lead Halide Perovskites ($CsPbX_3$, X= Cl, Br, and I): Novel Optoelectronic Materials Showing Bright Emission with Wide Color Gamut. *Nano Lett.* **2015**, *15*, 3692–3696.
35. Zhou, L.; Xu, Y. F.; Chen, B. X.; Kuang, D. B.; Su, C. Y. Synthesis and Photocatalytic Application of Stable Lead-Free $Cs_2AgBiBr_6$ Perovskite Nanocrystals. *Small* **2018**, *14*, 1703762.
36. Zhang, Y.; Yin, J.; Parida, M. R.; Ahmed, G. H.; Pan, J.; Bakr, O. M.; Brédas, J. L; Mohammed, O. F. Direct-Indirect Nature of the Bandgap in Lead-Free Perovskite Nanocrystals. *J. Phys. Chem. Lett.* **2017**, *8*, 3173–3177.
37. Li, Z. J.; Hofman, E.; Li, J.; Davis, A. H.; Tung, C. H.; Wu, L. Z.; Zheng, W. W. Photoelectrochemically Active and Environmentally Stable $CsPbBr_3/TiO_2$ Core/Shell Nanocrystals. *Adv. Funct. Mater.* **2018**, *28*, 1704288.
38. Zhang, H.; Liu, H.; Tian, Z. Q.; Lu, D. L.; Yu, Y.; Cestellos-Blanco, S.; Sakimoto, K. K.; Yang, P. D. Bacteria Photosensitized by Intracellular Gold Nanoclusters for Solar Fuel Production. *Nat. Nanotechnol.* **2018**, *13*, 900–905.
39. Miao, Q. Q.; Xie, C.; Zhen, X.; Lyu, Y.; Duan, H. W.; Liu, X. G.; Jokerst, J. V.; Pu, K. Molecular Afterglow Imaging with Bright, Biodegradable Polymer Nanoparticles. *Nat. Biotechnol.* **2017**, *35*, 1102–1110.
40. Pattengale, B.; Yang, S. Z.; Ludwig, J.; Huang, Z. Q.; Zhang, X. Y.; Huang, J. Exceptionally Long-Lived Charge Separated State in Zeolitic Imidazolate Framework:

DOI: 10.31635/ccschem.022.202101694
Citation: *CCS Chem.* **2023**, 5, 164–175
Link to VoR: https://doi.org/10.31635/ccschem.022.202101694

Implication for Photocatalytic Applications. *J. Am. Chem. Soc.* **2016**, *138*, 8072–8075.
41. Kornienko, N.; Zhang, J. Z.; Sakimoto, K. K.; Yang, P. D.; Reisner, E. Interfacing Nature's Catalytic Machinery with Synthetic Materials for Semi-Artificial Photosynthesis. *Nat. Nanotechnol.* **2018**, *13*, 890–899.
42. Zhou, J. J.; Huang, J.; Xia, Y.; Ou, H.; Li, Z. J. Two-in-One Ultraviolet Persistent Luminescent Catalyst Suitable for High Concentration Photodegradation. *Sci. Total Environ.* **2020**, *699*, 134342.
43. Cui, G. W.; Yang, X. L.; Zhang, Y. J.; Fan, Y. Q.; Chen, P.; Cui, H. Y.; Liu, Y.; Shi, X. F.; Shang, Q. Y.; Tang, B. Round-the-Clock Photocatalytic Hydrogen Production with High Efficiency by a Long-Afterglow Material. *Angew. Chem. Int. Ed.* **2019**, *58*, 1340–1344.
44. Zhang, S. H.; Shi, J. F.; Sun, Y. Y.; Wu, Y. Z.; Zhang, Y. S.; Cai, Z. Y.; Chen, Y. X.; You, C.; Han, P. P.; Jiang, Z. Y. Artificial Thylakoid for the Coordinated Photoenzymatic Reduction of Carbon Dioxide. *ACS Catal.* **2019**, *9*, 3913–3925.
45. Sakimoto, K. K.; Wong, A. B.; Yang, P. D. Self-Photosensitization of Nonphotosynthetic Bacteria for Solar-to-Chemical Production. *Science* **2016**, *351*, 74–77.
46. Light, S. H.; Su, L.; Rivera-Lugo, R.; Cornejo, J. A.; Louie, A.; Iavarone, A. T.; Ajo-Franklin, C. M.; Portnoy, D. A. A Flavin-Based Extracellular Electron Transfer Mechanism in Diverse Gram-Positive Bacteria. *Nature* **2018**, *562*, 140–144.

DOI: 10.31635/ccschem.022.202101694
Citation: *CCS Chem.* **2023**, 5, 164–175
Link to VoR: https://doi.org/10.31635/ccschem.022.202101694